RSC Advances

ROYAL SOCIETY OF CHEMISTRY

PAPER

View Article Online
View Journal | View Issue

Cite this: *RSC Adv.*, 2025, **15**, 16677

Microstructures and anomalous magnetic properties of C@Ni–NiO nanoparticles synthesized by a homogeneous precipitation method †

Zhen-Fei Yu,[a] Kun-Yu Su,[b] Duan-Qing Chen,[b] Yu-Ru Ding,[a] Yi Zhang,[c] Wei Zhong *[d] and Xue-Min He *[ad]

Received 28th March 2025
Accepted 8th May 2025

DOI: 10.1039/d5ra02174j

rsc.li/rsc-advances

Uniformly dispersed nano-sized C@Ni(OH)$_2$ microspheres were obtained *via* a solvothermal reaction and homogeneous precipitation method, and were subsequently calcined in argon atmosphere to produce C@Ni–NiO nanoparticles. The microstructure and proportion of Ni and NiO in the samples varied with solvothermal temperatures (160 °C and 180 °C) and calcination temperatures (600 °C and 800 °C). Four representative C@Ni–NiO samples with NiO content of 8.2%, 27.7%, 38.1%, and 16.9%, respectively, were selected as the objects of microstructural and magnetic research. The phase composition and morphology of nanocomposites were analyzed by XRD, XPS, SEM and TEM, and the magnetic properties at room temperature and low temperature were measured using SQUID. The results show that small and uniform Ni–NiO particles were attached to carbon spheres with certain aggregation, and the average crystallite sizes of Ni and NiO phases for these four samples were less than 80 nm and 20 nm, respectively. Room-temperature coercivity was 67 Oe, 48 Oe, 77 Oe, and 49 Oe, respectively, and there are only two samples that showed a slight increase (8 Oe and 9 Oe) in coercivity at 5 K after field cooling. The C@Ni–NiO samples exhibited weak exchange bias ($\leq$30 Oe), which was attributed to the low anisotropy of antiferromagnetic NiO. The influences of particle size, phase content, and interface effect on the magnetic properties were further analyzed in this work.

1 Introduction

With the development of nanotechnology, particle systems composed of 3d transition metals and their oxides, such as Fe/FeO, Co/CoO, and Ni/NiO, have been widely studied due to their numerous applications in magnetic fluids,[1] magnetic recording media,[2] biomedicine,[3] catalysis,[4] *etc.* In particular, the Co/CoO core–shell nanocomposite system exhibited a remarkable exchange bias effect, which can beat the superparamagnetic limit in magnetic recording media and enhance the performance of permanent magnetic materials.[5,6] The exchange bias (EB) arises from the exchange coupling at the interface between the ferromagnetic (FM) and antiferromagnetic (AFM) components. The effects induced by this FM–AFM exchange coupling include domain wall pinning, enhancement of coercivity, and unidirectional anisotropy. In materials composed of a FM–AFM interface, the Néel temperature (T_N) associated with the AFM component is often lower than the Curie temperature (T_C) associated with the FM component.

By cooling the sample under an applied field from temperatures above T_N, a hysteresis loop measurement conducted at low temperatures reveals a shift of the loop along the field axis. The magnitude of this shift is known as the exchange bias field (H_E).[7,8] The Ni–NiO system is suitable for studying exchange bias. Firstly, NiO, unlike typical 3d transition metal oxides such as CoO (293 K) and FeO (198 K), exhibits a higher T_N of 523 K. This allows the Ni–NiO system to generate EB effect even at room temperature. Secondly, compared with Fe and Co nanoparticles that are more susceptible to oxidation in air, handling Ni nanoparticles is much easier and safer.[9,10] Therefore, investigating the exchange bias in Ni/NiO systems is not only significant for understanding the magnetic hysteresis loop itself but also for other related phenomena associated with exchange bias.

The magnetic properties of Ni–NiO nanocomposite are primarily determined by the microstructural characteristics of the two components and the interface (*e.g.*, contact mode, area, roughness, *etc.*). These factors are crucial, especially at the nanoscale, and are strongly influenced by the synthetic routes utilized.[11,12] In recent years, significant progress has been made

---

[a] *Jiangsu Provincial Engineering Research Center of Low Dimensional Physics and New Energy, College of Science, Nanjing University of Posts and Telecommunications, Nanjing 210023, China. E-mail: hxm@njupt.edu.cn*

[b] *College of Electronic and Optical Engineering, Nanjing University of Posts and Telecommunications, Nanjing 210023, China*

[c] *Department of Physics, Mathematics & Science College, Shanghai Normal University, Shanghai 200234, China*

[d] *National Laboratory of Solid State Microstructures, Nanjing University, Nanjing 210093, China. E-mail: wzhong@nju.edu.cn*

† Electronic supplementary information (ESI) available. See DOI: https://doi.org/10.1039/d5ra02174j

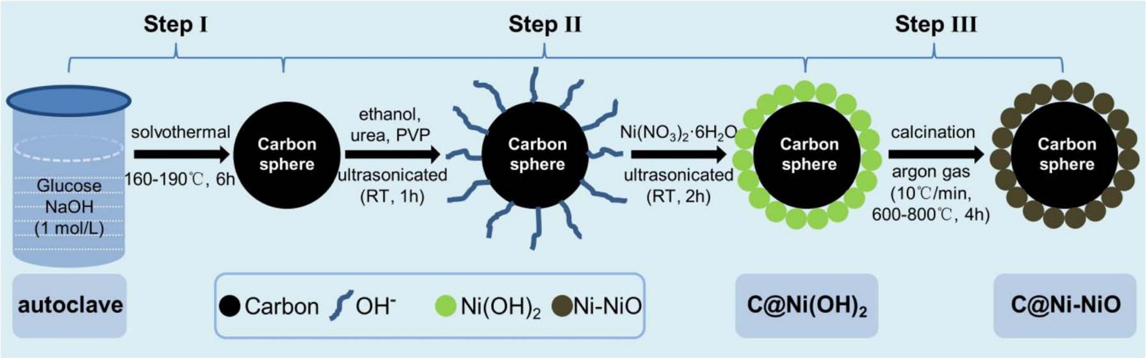

Fig. 1 Synthesis schematic of C@Ni–NiO nanoparticles.

in the synthesis of Ni/NiO binary artificial particles using chemical methods such as co-precipitation,[13] sol–gel,[14] thermal decomposition,[15] and solvothermal.[16,17] These chemical synthesis methods facilitate effective control over the microstructure. As a typical carbon material, carbon spheres (CS) possess advantages such as easy preparation and controllable morphology, while also retaining the benefits of other carbon materials. Additionally, the carbon spheres with uniform surface energy, due to their spherical shape, can aid in the uniform dispersion and coating of nanoparticles on the surface. As a carrier, the carbon spheres possess high specific surface area and good conductivity, which can provide a large number of catalytic active sites and electron transfer channels. The stable contact between the nanoparticles and highly conductive carbon spheres are expected to compensate for the insufficient electron conductivity of oxide nanoparticles.[18–20]

Herein, C@Ni–NiO nanoparticles of different sizes were prepared *via* a homogeneous precipitation method. We systematically investigated their microstructure and magnetic properties using comprehensive characterization techniques. The effects of particle size, phase content, and interface on magnetic properties, such as saturation magnetization (M_s), coercivity (H_C), exchange bias (H_E), and blocking temperature (T_B), were thoroughly analyzed. As a result, the C@Ni–NiO nanoparticles exhibited a weak H_E and enhanced H_C.

2 Experimental section

2.1 Sample preparation

The raw materials utilized are glucose, sodium hydroxide, nickel nitrate hexahydrate ($Ni(NO_3)_2 \cdot 6H_2O$), urea, polyvinylpyrrolidone (PVP), anhydrous ethanol, and deionized water. All the aforementioned materials are analytical grade purity. In a typical synthesis process, the pH value of glucose solution was adjusted to alkaline with 1 mol per L sodium hydroxide solution. The solvothermal reaction was carried out at temperatures exceeding 150 °C for 6 hours. After cooling to room temperature, the product was washed several times with a mixture of deionized water and ethanol, and then dried under vacuum at 50 °C for 12 hours to obtain a dark brown powder (namely the carbon spheres).

The carbon spheres were dispersed in anhydrous ethanol, followed by the addition of an appropriate amount of urea and PVP. The dispersion was sonicated for 1 hour, and then a specific amount of nitric acid solution of $Ni(NO_3)_2 \cdot 6H_2O$ was added. The dispersion was further sonicated for 2 hours, resulting in a deep brown suspension. After cooling and settling, the resultant substance was washed three times with anhydrous ethanol and deionized water, respectively. The obtained powder was dried at 80 °C and eventually the C@Ni(OH)$_2$ microsphere sample was formed.

The powder of C@Ni(OH)$_2$ microsphere was then subjected to calcination in a tube furnace at a certain temperature under an argon atmosphere with a specific heating rate. The calcination process was maintained at the target temperature for 4 hours, followed by cooling and grinding to obtain the powdered sample of C@Ni–NiO nanoparticles. Fig. 1 shows the synthesis schematic of C@Ni–NiO nanoparticles.

In the experiment, in addition to changing the temperature of solvothermal reaction (160 °C, 170 °C, 180 °C, 190 °C), the calcination temperature (400 °C, 500 °C, 600 °C, 700 °C, 800 °C) was also changed to obtain several series of samples in order to

Table 1 Microstructural and magnetic parameters of four representative C@Ni–NiO samples (M1–M4) prepared at different solvothermal temperatures (T_1) and calcination temperatures (T_2)

				Ni & NiO		M_s (emu g^{-1}) & H_C (Oe)	ΔH_C (Oe) & H_E (Oe)
No.	T_1 (°C)	T_2 (°C)	T_B (K)	Crystallite size (nm)	Content (%)	$T = 300$ K	$T = 5$ K
M1	160	800	270	73.8 & 16.0	91.8 & 8.2	17.9 & 67	8 & 12
M2	180	800	240	56.5 & 13.7	72.3 & 27.7	7.4 & 48	9 & 30
M3	160	600	220	53.3 & 14.3	61.9 & 38.1	13.9 & 77	0 & 0
M4	180	600	270	64.0 & 14.6	83.1 & 16.9	8.8 & 49	0 & 3

control the microstructure of C@Ni–NiO nanoparticles. For better comparative analysis, in the subsequent study related to microstructural and magnetic characterizations, we focus on the C@Ni–NiO samples prepared at solvothermal temperatures of 160 °C and 180 °C, and calcination temperatures of 800 °C and 600 °C. As shown in Table 1, the four samples are named M1–M4 respectively.

2.2 Microstructural characterization

X-ray diffraction (XRD) pattern was determined using a Philips X'pert diffractometer equipped with a rotating anode and Cu Kα radiation (40 kV, 40 mA, $\lambda = 1.5406$ Å). Based on the information of the standard cards, the data from the XRD analysis were subsequently refined using the GSAS program, and thus microstructural parameters such as the average crystallite size, the lattice constant, and the phase content can be obtained. X-ray photoelectron spectroscopy (XPS) was performed using a Kratos Axis Ultra DLD spectrophotometer with an Al Kα radiation source. The particle shape was imaged with a FEI Sirion200 scanning electron microscope (SEM) operating at an accelerating voltage of 5 kV. For transmission electron microscope (TEM) investigation, a drop of the tested powder sample in ethanol was deposited on each carbon-coated copper grid and then dried in air. Based on the JEOL JEM-2100 instrument, high-resolution TEM (HRTEM) in conjunction with selected-area electron diffraction (SAED) analyses were used to determine the local microstructure and crystallographic phase.

2.3 Magnetic measurement

Based on the MPMS-XL superconducting quantum interference device (SQUID), the magnetic properties were recorded for powder sample, and the magnetization was measured against the magnetic field and the temperature. More specifically, it mainly including the following three aspects: (i) SQUID measured room-temperature hysteresis (M–H) loop in a magnetic field up to ±65 kOe; (ii) low-temperature ($T = 5$ K) M–H loop under zero-field-cooling (ZFC) and field-cooling (FC, from 350 K in a field of $H_{\text{cool}} = 30$ kOe); and (iii) ZFC and 500 Oe FC magnetization (M–T) curves in the range 2–350 K.

3 Results and discussion

3.1 Microstructural analysis

The XRD pattern of the final sample is shown in Fig. 2(a). From this pattern, three pieces of information can be obtained. Firstly, the broad hump near $2\theta = 22°$ obscures the low-intensity diffraction peaks of the sample, and its intensity indicates that the main component in the sample is still amorphous carbon. Secondly, the low-temperature calcination at 400 °C led to the formation of Ni as the predominant phase observed in all samples. This is attributed to the reduction of the majority of NiO, which is decomposed by carbon from $Ni(OH)_2$. Three distinct Bragg peaks were identified to correspond to (111), (200), and (220) planes of Ni phase. Finally, both Ni and NiO diffraction peaks are broad and low intensity. It indicates that the grains of Ni and NiO are very small and estimates to be in the nanometer range. Therefore it can be concluded that the obtained sample is actually a composite phase of C@Ni–NiO.

The XRD pattern obtained when the calcination temperatures are 600 °C and 800 °C is shown in Fig. 2(b). It is shown that they are face-centered cubic (fcc) in structure. It can be found that the signal of the sample is very strong and the peaks become sharp. This indicates that high-temperature calcination helps carbon reduce more NiO to Ni and is accompanied by grain growth.[21] Two sets of diffraction peaks suggest that the samples are composed of Ni and NiO phases. Among them, the three obvious peaks at 44.495°, 51.848° and 76.245° are corresponding to the (111), (200) and (220) crystalline planes of Ni (JCPDS card no. 97-2265), and the other three weak diffraction peaks at 37.043°(111), 43.038°(220) and 62.496°(220) matches with NiO phase (JCPDS card no. 97-3930). Obviously, both Ni and NiO phases have face-centered cubic (fcc) crystal structure with $Fm\bar{3}m$ (225) space group. Based on this, the microstructural parameters such as the average crystallite size and lattice

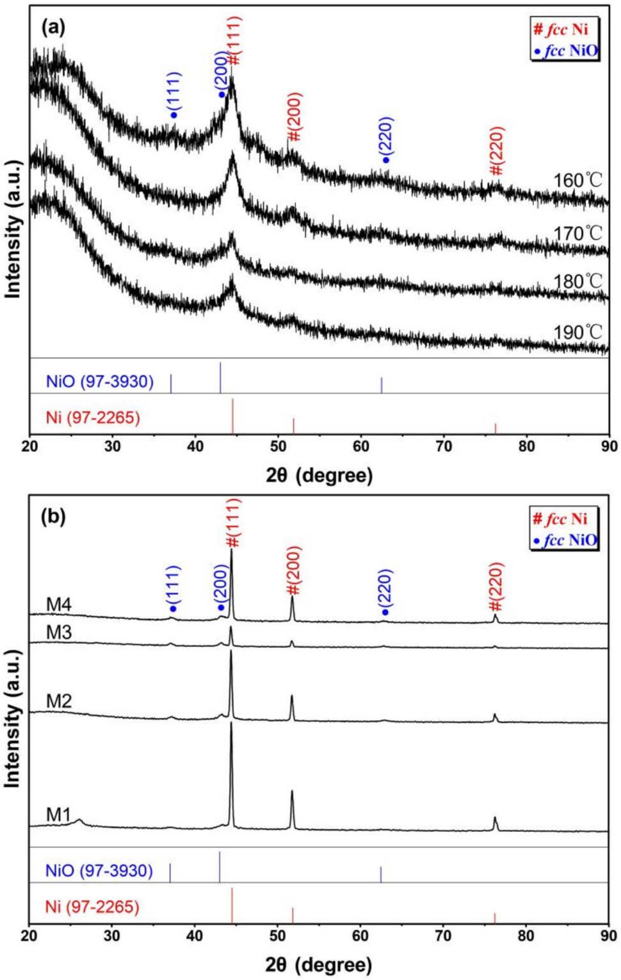

Fig. 2 (a) XRD patterns of C@Ni–NiO nanoparticles prepared at calcination temperature of 400 °C, according to the calcination of C@$Ni(OH)_2$ microspheres synthesized in solvothermal temperatures of 160–190 °C; (b) XRD patterns of samples M1–M4 formed in certain solvothermal temperatures (160 °C and 180 °C) and calcination temperatures (600 °C and 800 °C).

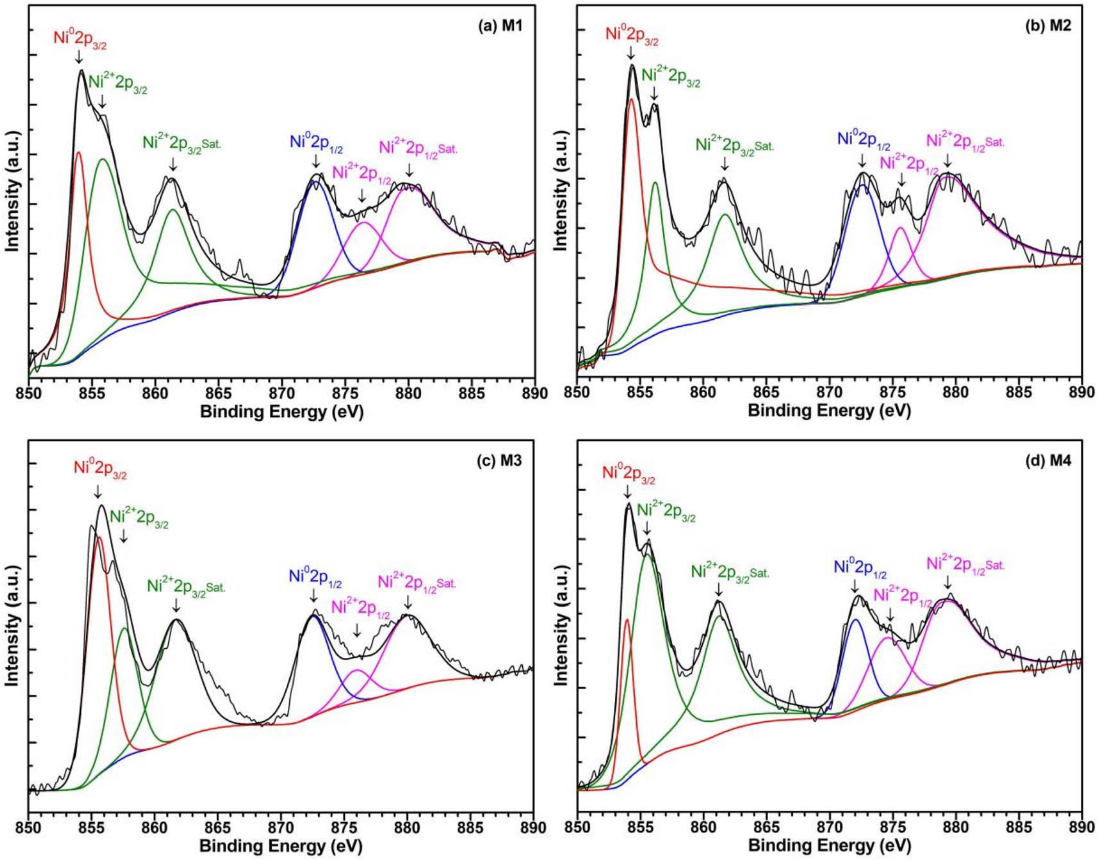

Fig. 3 XPS spectrum displaying the deconvoluted results of Ni 2p region for the sample (a) M1, (b) M2, (c) M3, and (d) M4.

constant of the two phases can be determined according to the XRD refinement (see Fig. S1, ESI†).

As shown in Table 1, the average sizes of Ni and NiO crystallites for the four samples are 61.9 nm and 14.7 nm, respectively. It can be observed that with an increase in the relative content of the phase, the grain size correspondingly increases. This could be attributed to a decrease in the number of grain boundaries due to the increase in the relative content of the phase, leading to an increase in grain size.[22] The average lattice constants of the Ni phase and NiO phase in the four samples are calculated to be 3.526 Å and 4.181 Å, slightly larger than 3.523 Å for bulk Ni and 4.177 Å for bulk NiO. Clearly, both the Ni and NiO phases exhibit a certain degree of lattice expansion. This could be attributed to factors such as lattice distortion or size effect, leading to a smaller volume and an increase in lattice constants.[23–25] Further analysis of the XRD data was processed with the refinement method using the GSAS program, to estimate the relative content of Ni and NiO phases in the Ni/NiO nanoparticles. The M1–M4 samples have a relative content (wt%) of NiO phase of 8.2%, 27.7%, 38.1% and 16.9%, respectively.

In order to assess the chemical charge states of Ni element in the synthesized nanoparticles, XPS characterization was employed. To get more information, the XPS data has been analyzed by the deconvolution method and the results are shown in Fig. 3. Obviously, the Ni 2p spectra obtained from the four samples can be divided into two spin–orbit coupling regions, namely Ni $2p_{3/2}$ (850–868 eV) and Ni $2p_{1/2}$ (868–890 eV).

Focus on the Ni $2p_{3/2}$ core-level spectrum, three nickel species have been reported: (i) metallic Ni appearing at a binding energy value of 853–855 eV, (ii) NiO with binding energy values in the range of 855–857 eV, and (iii) satellite peaks corresponding to Ni^{2+} at around 861–863 eV.[26–31] Concretely speaking, Ni $2p_{3/2}$ region is observed at 854.0 eV which corresponds to Ni^0 and 855.8 eV to Ni^{2+} oxidation state in sample M1. In sample M2, the peak is found at 854.3 eV (Ni^0) and Ni^{2+} oxidation state is found at 856.2 eV. In sample M3, the peak is found at 854.9 eV (Ni^0) and Ni^{2+} oxidation state is found at 856.7 eV. In sample M4, the peak is found at 854.0 eV (Ni^0) and Ni^{2+} oxidation state is found at 855.6 eV. Meanwhile, within the range of 860–865 eV, there are the shake-up satellite peaks of Ni^{2+} $2p_{3/2}$. The presence of the highly intense satellite peaks is consistent with the appearance of Ni^{2+} in the high-spin state, and the characteristic peak of $Ni(OH)_2$ has not been observed in the total XPS spectrum. This confirms the successful synthesis of C@Ni–NiO nanoparticles.

The typical SEM images in Fig. 4 reveal that the samples are spherical particles in submicron size. These particles have rough surface, which suggests that the microspheres are made up of smaller particles. The morphology of these four samples is very interesting, all of which are regular and uniform spheres. As shown in Fig. 4(c), the sample M3 obtained through 160 °C solvothermal treatment and subsequent 600 °C calcination exhibit porous spherical morphology with slight size variation. The porous structure is attributed to the reduction of NiO to Ni by certain carbons acting as reducing agents, resulting in the consumption of carbon from the carbon sphere template to form pores of varying sizes. The non-uniformity in size is mainly caused by the variation in size of the carbon sphere templates. When the calcination temperature is increased to 800 °C, as shown in Fig. 4(a), the porous spheres become more numerous and more uniform in size, which is due to the more complete reduction reaction under high-temperature calcination.[21] Furthermore, when larger carbon spheres were used as templates and solvothermal treatment was carried out at a temperature of 180 °C, it was astonishingly found that the yield of porous spheres increased significantly with more perfect shape and larger and more uniform size, as shown in Fig. 4(b) and (d). Many fine and homogeneous Ni–NiO nanoparticles were attached to the surface of the spheres, forming an appearance of hemp ball.

As a representative of the TEM images, Fig. 5(a) depicts the sizes of these nanoparticles for the C@Ni–NiO sample M1, clearly indicating the presence of Ni–NiO nanoparticles ranging from 10 nm to 200 nm in size, accompanied by a good cross between these particles. Obviously, such an HRTEM image of a selected region at the edge of one carbon sphere exhibits small and high-yield nanoparticles with good clarity. As shown in Fig. 5(a1), the high-resolution lattice image shows the [111] orientation of Ni phase and the [200] orientation of NiO phase in a single Ni–NiO nanoparticle, corresponding to interplanar spacings of 2.03 Å and 2.09 Å, respectively. Specifically, there is intersection of the lattice fringes of Ni and NiO. Fig. 5(a2) shows a typical SAED pattern corresponding to the C@Ni–NiO sample M1, consisting of some distinct concentric rings with discontinuous spots over the rings. As marked therein, the halo in the middle comes from amorphous carbon, and these diffraction rings appear due to reflections from (111) and (200) planes of the Ni phase for the composite structure.[28,32–34] The diffraction rings corresponding to the NiO phase were not observed. This is because the main phase in the sample is Ni, and the content of the NiO phase is very low (8.2%), which is consistent with the three obvious Bragg peaks of Ni in the XRD patterns. For the other three C@Ni–NiO nanoparticles samples (M2–M4), the TEM images of a few microspheres are shown in Fig. 5(b)–(d) and reveal a large gray area. It clearly indicates the presence of carbon spheres used as template. There is no dispute that, the small particles with relatively uniform size can also be observed, which is consistent with the results observed in SEM image. Of course, the absolute difference in microscopic morphology among the four samples is mainly influenced by the solvothermal temperature and the calcination temperature.

Based on the microstructural analysis above, this study validates the multiple advantages of the homogeneous precipitation method in the synthesis of C@Ni–NiO nanoparticles. Firstly, this method effectively controls particle size distribution and uniformity. SEM and TEM images reveal that the synthesized nanoparticles range in size from 10 nm to 200 nm and exhibit uniform morphology, and the rule is consistent with the nanoscale crystallite sizes obtained from XRD analysis. Compared to other synthesis methods such as sol–gel or hydrothermal routes, the homogeneous precipitation method through a gradual reaction process provides a more uniform particle distribution.[15,16,19] Secondly, the synthesis conditions of the homogeneous precipitation method (such as precursor concentration, pH value, and reaction temperature) enable precise control over the relative content of Ni and NiO phases. As shown in Fig. S1 (ESI)† and Table 1, XRD refinement analysis show that as the calcination temperature increases, the ratio of Ni to NiO phases changes significantly. For example, in the M1 sample prepared at calcination temperature of 800 °C, the Ni content is 91.8%, whereas in the M3 sample (600 °C-calcined), the Ni content is 61.9%. This ability to control phase ratios is a key advantage of the homogeneous precipitation method, especially in the synthesis of nanocomposites, where the phase composition can be adjusted to optimize material performance. Finally, the homogeneous precipitation method also demonstrates significant advantages in the crystallinity of particle interfaces. XPS, HRTEM and SAED analysis reveals well-defined crystalline interfaces between the Ni and NiO phases. This method can effectively control the crystallographic structure of the particles, and particularly, the highly consistent interfaces between Ni and NiO components are crucial for enhancing magnetic and catalytic properties in the composite materials. These advantages make the homogeneous precipitation method highly promising for the synthesis of composites, particularly in the design of magnetic materials and catalysts, where fine control over structure and properties is essential.

3.2 Magnetic analysis

The room-temperature (300 K) hysteresis loop of C@Ni–NiO nanoparticles was measured using SQUID, as shown in Fig. 6. These samples exhibit typical ferromagnetic properties, such as hysteresis, remanence, coercivity, and saturation. The occurrence of ferromagnetic behavior is not surprising, as the dominant phase in these samples is metallic Ni. Due to the varying content of NiO, specific magnetic parameter values differ among these samples. The absolute value of magnetization (M) cannot be directly measured, as the recorded weight during measurement is actually the weight of the carbon-based Ni–NiO nanoparticle powder sample, representing the macroscopic magnetism of the entire powder.

The saturation magnetization (M_s) values for samples M1–M4 are 17.9 emu g^{-1}, 7.4 emu g^{-1}, 13.9 emu g^{-1}, and 8.8 emu g^{-1}, respectively. The enlarged loops in the inset display corresponding coercivity values of 67 Oe, 48 Oe, 77 Oe, and 49 Oe. An interesting observation is that the hysteresis loops in the first and third quadrants of Fig. 6(c) do not saturate. The value of M actually decreases with increasing external magnetic field. This is due to the strong diamagnetic signal of carbon, which cannot be masked by the ferromagnetic properties of the sample itself. This explanation is supported by the SEM image in Fig. 4(c), which clearly shows the presence of a significant amount of carbon sphere templates in the samples.

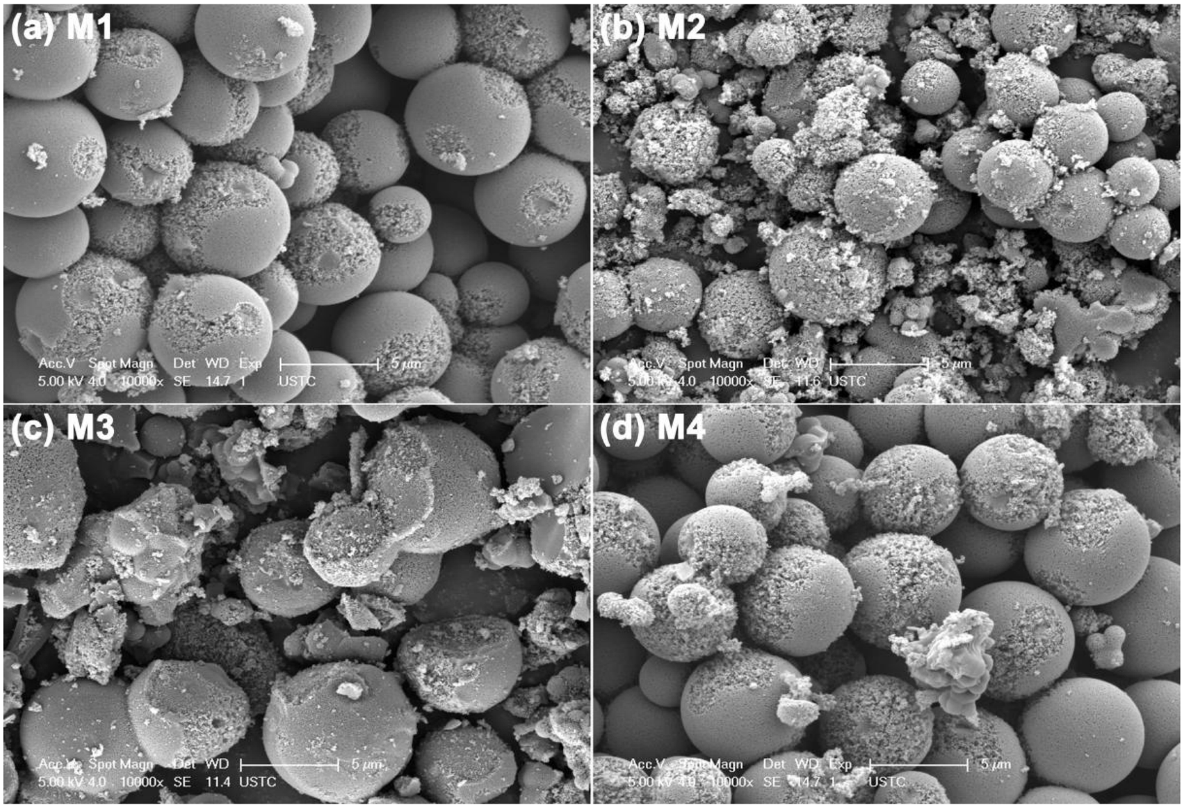

Fig. 4 SEM images of C@Ni–NiO samples M1 (a), M2 (b), M3 (c), and M4 (d).

To decrease the effect of thermal disturbance on magnetic properties, the hysteresis loops at 5 K were measured *via* zero-field cooling (ZFC) and field cooling (FC) using a SQUID magnetometer with 65 kOe maximum field, the results are shown in Fig. 7. The shape of the complete hysteresis loop suggests the presence of two components: ferromagnetic Ni and antiferromagnetic NiO. The linear portion with non-zero slope at high fields is attributed to antiferromagnetic NiO.[35,36] Considering the hysteresis loops under ZFC process, four samples still exhibit ferromagnetic behavior, similar to their overall characteristics at room temperature. However, there are significant changes observed in various magnetic parameters,

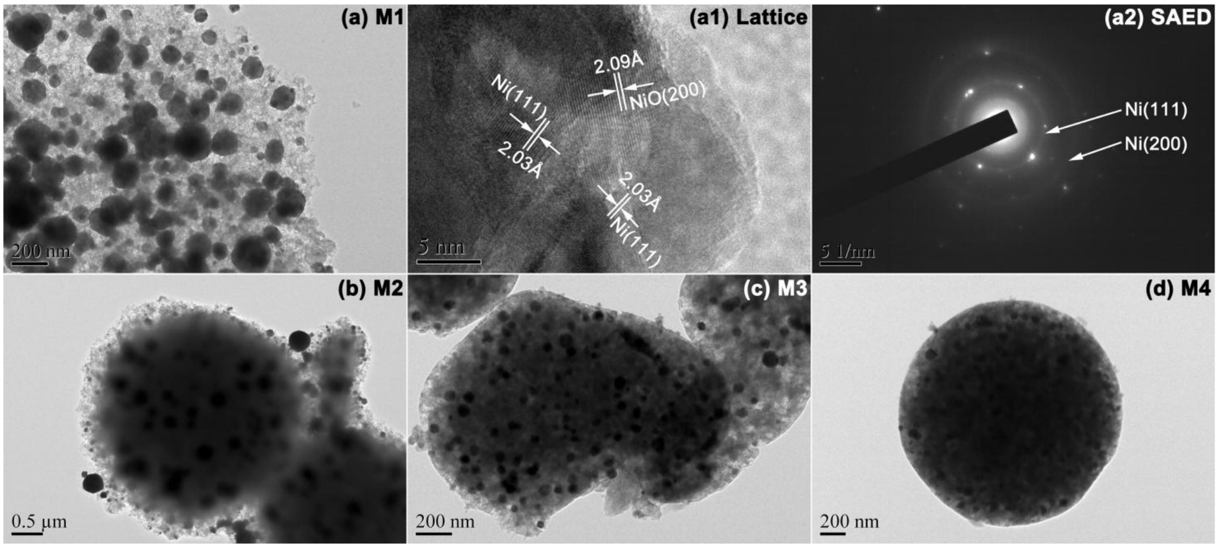

Fig. 5 TEM images of C@Ni–NiO samples M1 (a), M2 (b), M3 (c), and M4 (d); (a1) and (a2) represent the high-resolution lattice image and the SAED pattern of the sample M1, respectively.

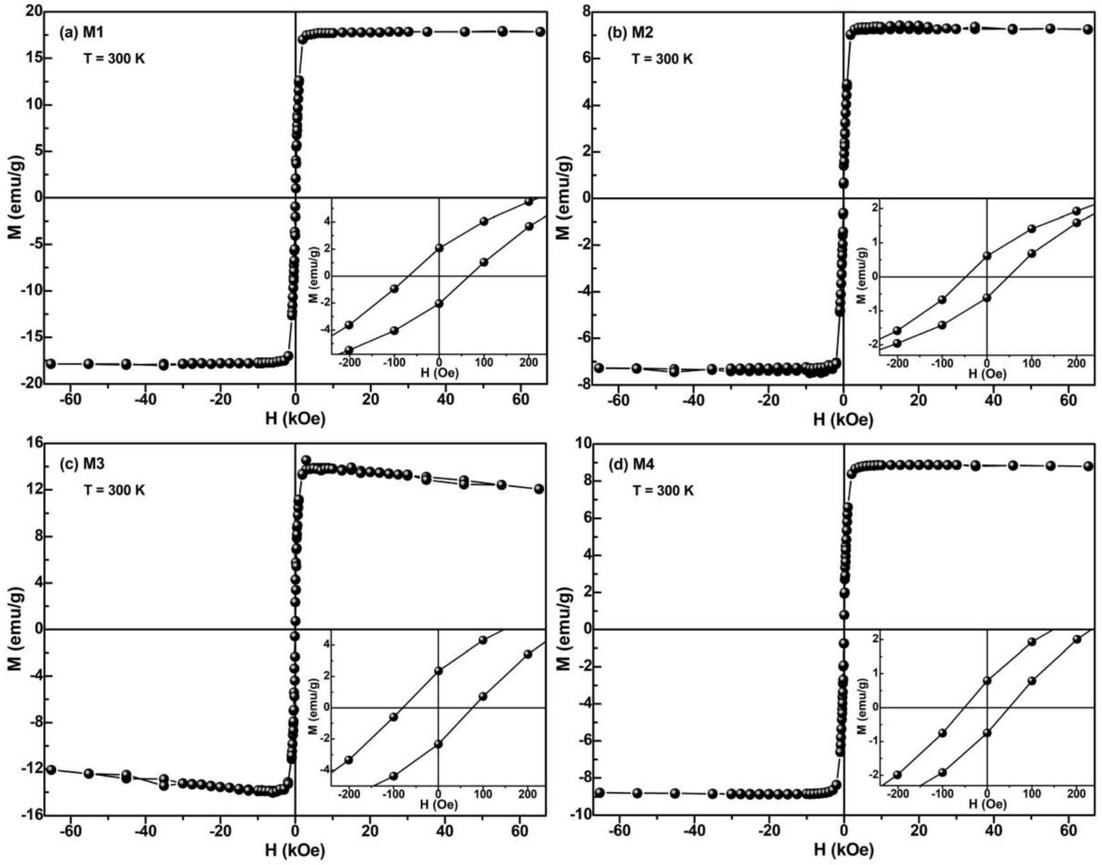

Fig. 6 Hysteresis loops at room temperature for the C@Ni–NiO sample (a) M1, (b) M2, (c) M3 and (d) M4, the inset shows an enlargement of the low-field region of the loop to display the coercivity and remanence.

particularly an increase in the M_s compared to its value at room temperature. This can be primarily attributed to the reduction of thermal disturbance at low temperatures, allowing for a greater alignment of magnetic moments with the direction of the magnetic field.[37] At 5 K, the values of M_s for the four samples are 19.2 emu g^{-1}, 7.9 emu g^{-1}, 15.3 emu g^{-1}, and 9.8 emu g^{-1}, respectively. The enlarged loops in the inset show that the corresponding coercivity values are 272 Oe, 294 Oe, 250 Oe, and 224 Oe at ZFC process. Among the four samples, the M_s value of sample M2 exhibits a slight decrease, which may be attributed to a reduced proportion of the Ni component in its structure or variations in particle size, resulting in a decreased number of effective magnetic moments that can be aligned by the applied field. Overall, the hysteresis behavior under ZFC conditions reveals the complex magnetic interaction mechanisms of the samples in a low-temperature environment.

Moreover, as shown in Fig. S2 (ESI),† the hysteresis loop of pure Ni/NiO nanocomposites (without carbon support) at 5 K was also measured. Compared to pure Ni/NiO, the C@Ni–NiO samples M1–M4 exhibit an appreciable decrease in coercivity. This suggests that the carbon support helps reduce the aggregation of Ni–NiO particles, enhancing their dispersion and stability, and promoting more magnetic ions to participate in the magnetic response. Specifically, under an applied magnetic field, more particles are able to reach magnetic saturation. As carbon itself is non-magnetic, and the interface between carbon and Ni–NiO may influence the magnetic interactions, the coupling between particles is weakened, resulting in a reduction in the width of the hysteresis loop and, consequently, a decrease in coercivity.

The sample M3 still exhibits a similar behavior to that at room temperature, with descending loops in the first and third quadrants, which can also be attributed to the diamagnetic behavior of a significant portion of carbon spheres in the sample. The M_s value under FC is the same as that under ZFC. However, there are still differences between the FC and ZFC loops, particularly for samples M1 and M2. Also at 5 K, the coercivity values under FC process are 280 Oe, 303 Oe, 250 Oe, and 224 Oe for the four samples, respectively. Compared to the ZFC condition, the coercivity slightly increases for M1 and M2, with H_C increasing by 8 Oe and 9 Oe, respectively, while M3 and M4 remain unchanged. As shown in Fig. 7(c) and (d), the two loops perfectly overlap from the enlarged loops. From the 30 kOe FC loops shown in Fig. 7(a) and (b) can be seen that the values of H_E for samples M1 and M2 are 12 Oe and 30 Oe, respectively. The FC hysteresis loop in Fig. 7(b) is unsaturated and linearly increases with the rise in external magnetic field, largely due to the coupling interaction between ferromagnetic Ni and antiferromagnetic NiO components. Moreover, this coupling effect facilitates multiple spin reversal pathways

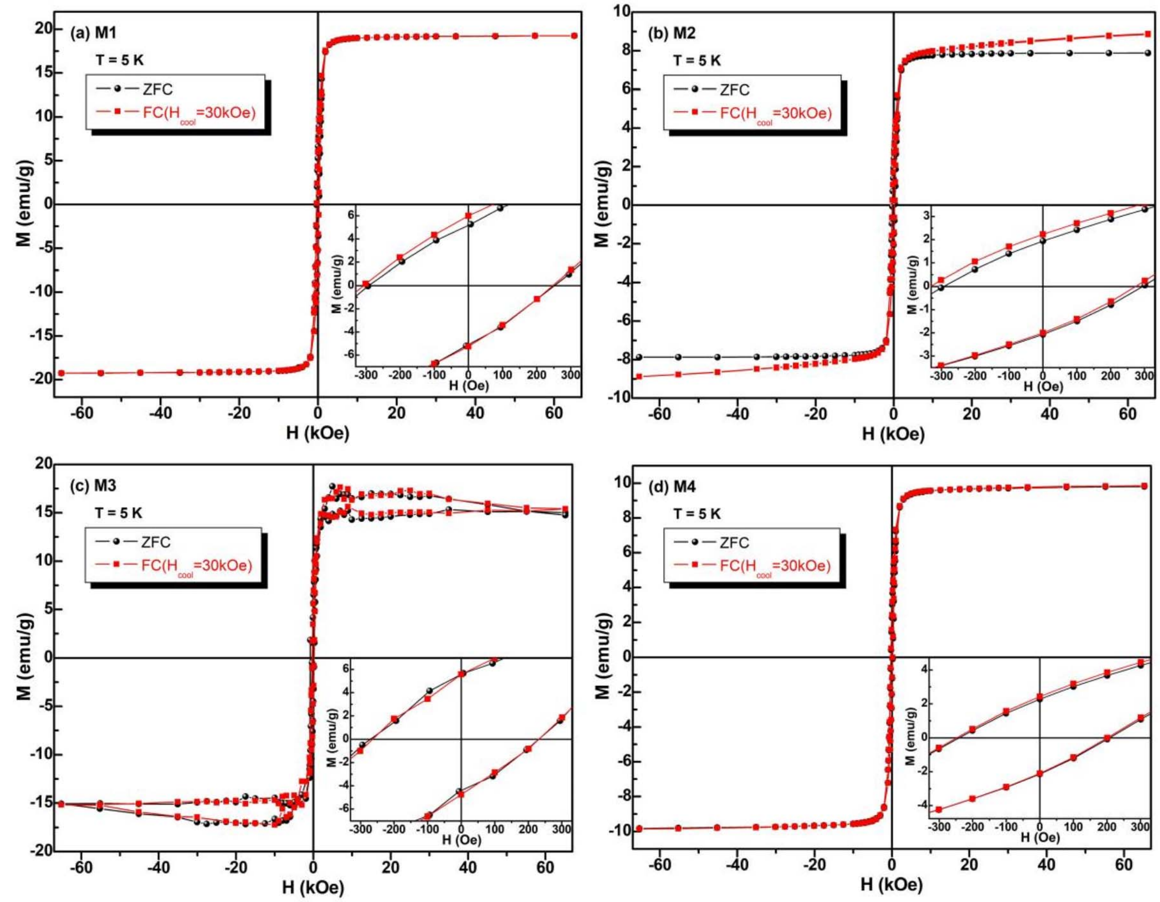

Fig. 7 Hysteresis loops at 5 K for the C@Ni–NiO sample (a) M1, (b) M2, (c) M3 and (d) M4 after ZFC and FC (from 350 K in a cooling field of 30 kOe) processes; the inset shows an enlargement of the low-field region of the loop to display the remanence, coercivity, and exchange bias.

during the magnetization ascension, leading to an enhanced coercivity.[38–42]

Compared to many other FM/AFM systems that exhibit large exchange bias,[43–51] these Ni–NiO composite nanoparticles indeed show a very weak exchange bias. However, among all the Ni–NiO systems reported in the literature, exchange bias is generally small, and some even have no exchange bias, just like samples M3 and M4.[52–57] In the Ni–NiO nanoparticles system documented in the literature, no notable shift of the hysteresis loop was observed, even at temperatures significantly lower than the blocking temperature (T_B). The observed coercivity values were only approximately 50–200 Oe, which is attributed to the low anisotropy of the antiferromagnetic NiO. Thus, for the sample M2, the emergence of maximum exchange bias coincides with an increase in coercivity. In contrast to the other three samples, it displays the highest H_E and ΔH_C. This is ascribable to the high content of antiferromagnetic NiO in sample M2. Although the M3 sample has a higher content of NiO, the presence of non-magnetic carbon (in its amorphous form) in the system acts as a spacer, potentially suppressing the exchange coupling between FM and AFM components, which results in an observed absence of exchange bias in the sample M3.[58] In addition, the ZFC and FC loops of sample M3 exhibit a large difference in the saturation magnetization between the upper and lower branches, which is due to the presence of carbon reducing the saturation magnetization of the sample M3. As a result, the magnetic moment of sample M3 cannot reach a high saturation state under the same applied magnetic field.[59] The literature further validates the aforementioned phenomenon.[60] Thakur *et al.* studied the hysteresis loops of Ni/NiO nanoparticles prepared by the sol–gel method and observed typical exchange bias effects under field-cooling conditions.[60] During the cooling process, the horizontal shift of the hysteresis loop was positively correlated with the decrease in particle size, while the vertical shift remained nearly unchanged. This observation is consistent with our findings, indicating that the exchange interaction between the ferromagnetic Ni and the antiferromagnetic NiO at the Ni/NiO interface is the key factor responsible for the loop shift. Moreover, although the exchange bias effect is generally weak in Ni/NiO systems, its strength is still closely related to the sample's structure and cooling process, further supporting the magnetic differences observed under different cooling conditions in our study.

The temperature dependence of magnetization in ZFC and FC modes is illustrated in Fig. 8, where the magnetic behavior disclosed by ZFC and FC magnetizations sheds light on the Ni/

NiO system. The ZFC/FC curves exhibit irreversible magnetic behavior in the entire temperature range of 2 K to 350 K (depicted by the splitting of FC and ZFC curves), with irreversibility occurring in all curves for $T > 300$ K. This behavior indicates a strong FM/AFM exchange coupling within the particulate system.

As the temperature rises, M_{ZFC} increases, while M_{FC} decreases conversely. The change in M_{FC} is less prominent than that of M_{ZFC}, which can be interpreted by the thermally activated process of FM torque. After ZFC, the particle magnetic moments tend to be randomly arranged at lower temperatures. As the temperature increases, FM torques attempt to align in the direction of the applied field, consequently causing the net magnetization to gradually increase. With cooling restoration, FM remains locked in the magnetic field direction. Thus, compared to ZFC magnetization, FC magnetization does not experience significant change upon decreasing temperature.[35,61] For the ZFC process, M_{ZFC} rapidly increases with rising temperature before reaching a particular peak value, after which it slowly decreases. This occurs because when the temperature is elevated and a magnetic field is applied, the magnetic moments swiftly increase and reach a maximum value near the blocking temperature (T_B), before gradually losing their orderly arrangement at higher temperatures. The rise in thermally excited magnetic moments renders their directions more random, resulting in a gradual decline in magnetization. The maximum value of the ZFC curve provides the average T_B of the samples. To showcase the information of the ZFC curve peak values, Fig. 8 offers a clear inset, demonstrating the peak temperatures of the four samples to be 270 K, 240 K, 220 K, and 270 K. The variance in peak temperatures is primarily caused by the different dimensions of the four samples. Moreover, the sample M4 displays a second peak temperature at a slightly higher temperature of 340 K. The Néel temperature signifies the transition temperature from antiferromagnetic to paramagnetic phase for NiO. As we cool below this temperature, the antiferromagnetic properties of the NiO layer enhance with a decrease in temperature, causing this peak. The second peak temperature at 340 K is associated with the loss of ferromagnetic order in Ni, which acts as the magnetic damping temperature of Ni nanodomains, signifying a significant weakening of the magnetic properties. This phenomenon is manifested during the cooling process due to the formation of new ordered ferromagnetic zones.

The temperature at which the ZFC and FC curves separate is termed as irreversibility temperature (T_{irr}), attributed mainly to the presence and distribution of magnetic anisotropy energy barriers. At any temperature below the onset of the bifurcation,

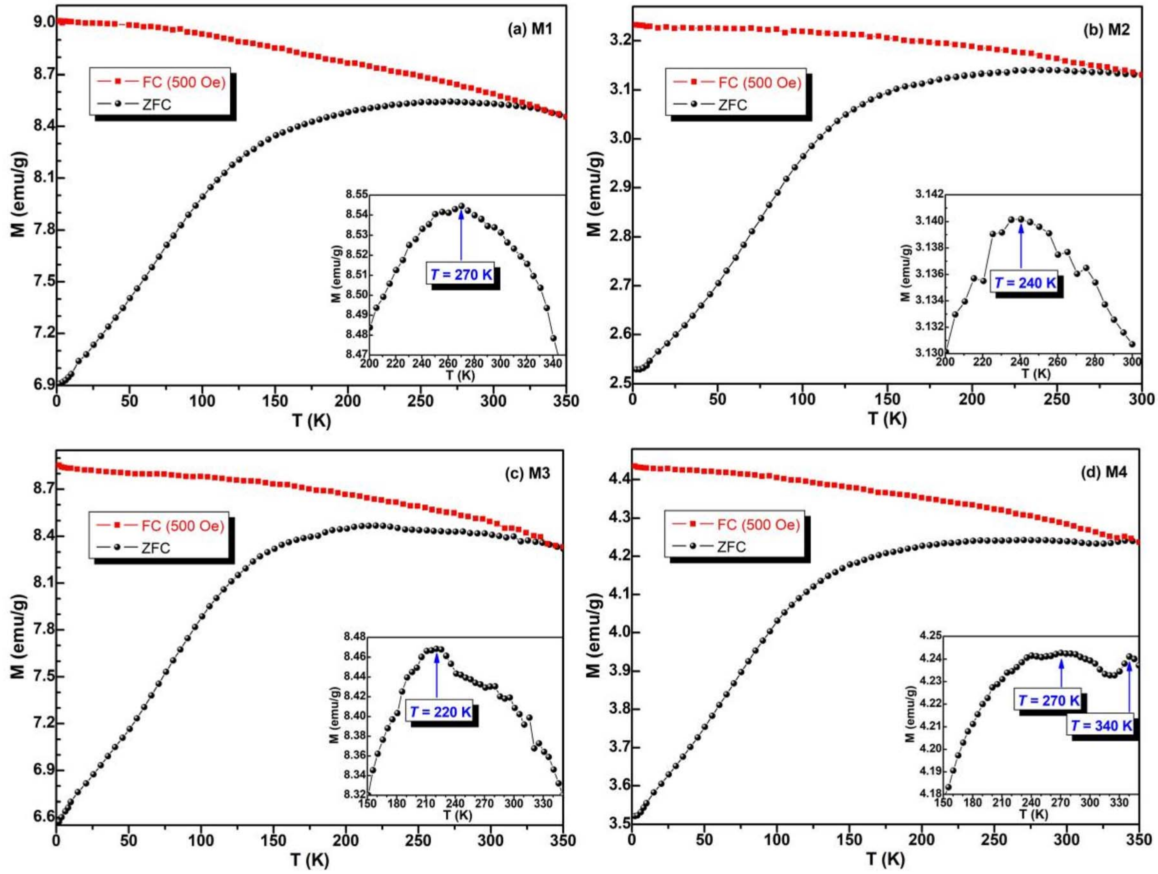

Fig. 8 Temperature dependence of ZFC/FC magnetization for the C@Ni–NiO sample (a) M1, (b) M2, (c) M3 and (d) M4; the inset depicts that the same ZFC curves in the temperature range of 150–350 K to show the peaks better.

the magnetization difference between FC and ZFC is non-zero, defined as irreversible magnetization $\Delta M = M_{\mathrm{FC}} - M_{\mathrm{ZFC}}$, indicating the degree of magnetization blocking. This magnetic irreversibility validates the existence of FM/AFM exchange coupling.[62] As shown in Fig. 9, the $M_{\mathrm{FC}} - M_{\mathrm{ZFC}}$ difference curve manifests the typical behavior of ferromagnetic materials (sharply dropping to zero post T_{B}). In temperatures above the T_{irr}, magnetic moments can freely rotate, causing overlapping ZFC and FC curves. However, when temperatures fall below the T_{irr}, magnetic moments are locked in a certain direction, causing a split in ZFC and FC curves. The split between ZFC and FC curves is due to the freezing of disordered uncompensated surface spins.[63]

Rinaldi-Montes *et al.* synthesized Ni/NiO core/shell nanoparticles by pyrolyzing inorganic precursors within the pores of an activated carbon matrix, followed by oxidation in air.[64] They found that the spins within the NiO shell froze into a spin-glass (SG) state at temperatures below T_{f} (~40 K). The magnetic exchange coupling between the Ni core and the spins in the NiO shell led to the emergence of EB effect, with its temperature dependence following a uniform exponential trend across all samples. Due to the SG nature of the shell spins, the EB effect disappears above T_{f}. This temperature is much lower than the T_{N} (~523 K) of antiferromagnetic NiO, which typically determines the starting temperature of the EB effect at the Ni/NiO interface. The magnetic properties of the Ni/NiO nanostructures are influenced not only by particle size and core/shell configuration but also by the SG state, interfacial exchange interactions, and thermal excitation processes. This suggests that the observed temperature-dependent magnetic behavior has broad universality in nanomaterials with similar core–shell structures.

In the vicinity of temperature T within the range of dT, the magnetization of pinned nanoparticles is given by $-\mathrm{d}(\Delta M)/\mathrm{d}T$. It is well known that T_{B} follows the relationship:[65]

$$T_{\mathrm{B}} = \frac{K_{\mathrm{a}} V}{25 k_{\mathrm{B}}}$$

where K_{a} represents the magnetic crystal anisotropy, V denotes the volume of the magnetic portion of the nanoparticles, and k_{B} is the Boltzmann constant. Considering that K_{a} is independent of temperature, T_{B} will solely depend on the volume of individual nanoparticles. Hence, the plot of $-\mathrm{d}(\Delta M)/\mathrm{d}T$ represents a function of particle volume density. The insets in Fig. 9 depict the corresponding $-\mathrm{d}(\Delta M)/\mathrm{d}T$–$T$ curves, reflecting the log-normal distribution of NiO nanoparticles.[66,67] The median T_{B} values for the four samples are 68 K, 69 K, 76 K, and 70 K, respectively.

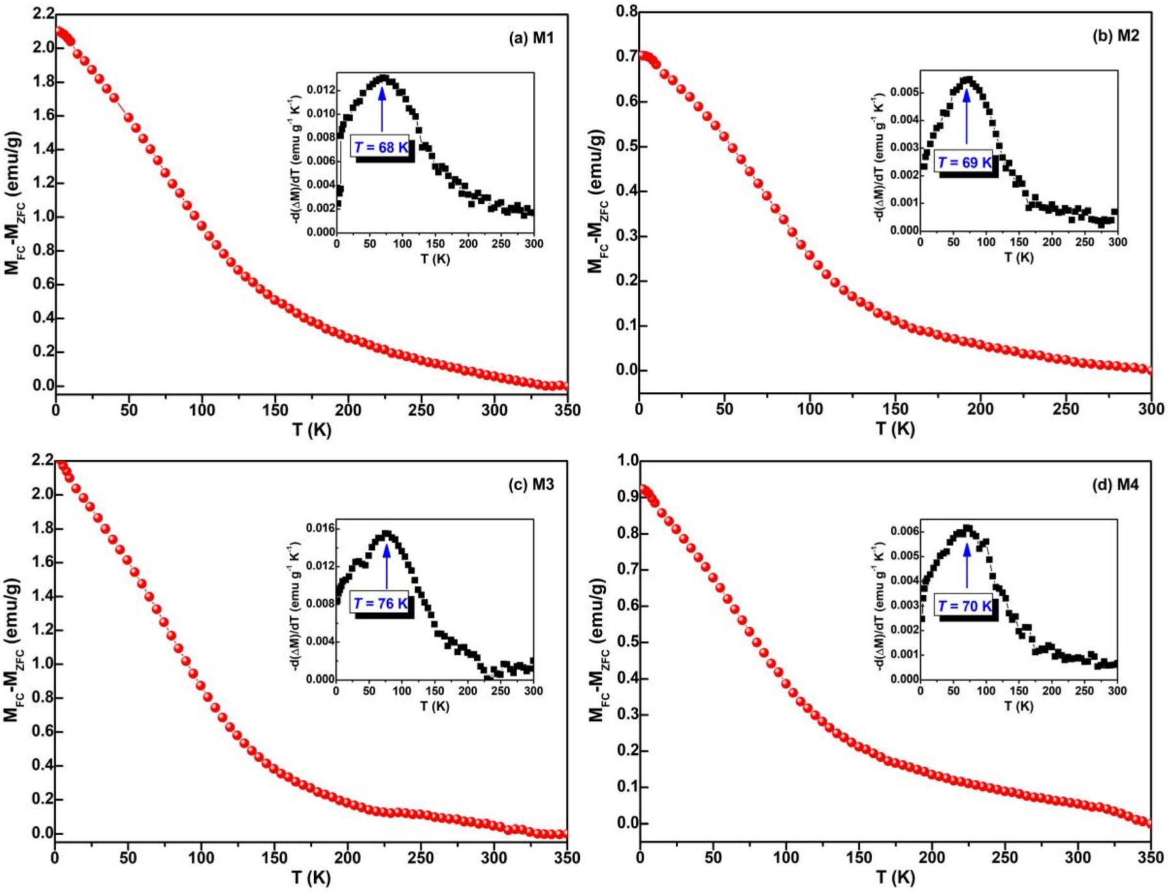

Fig. 9 The curves of $(M_{\mathrm{FC}} - M_{\mathrm{ZFC}})$–$T$ for the C@Ni–NiO sample (a) M1, (b) M2, (c) M3 and (d) M4; the inset shows $-\mathrm{d}(\Delta M)/\mathrm{d}T$–$T$ curve to display accurate median T_{B}.

In the case of magnetic nanoparticles, the blocking temperature is a significant parameter as it characterizes the transition from a superparamagnetic regime to a blocked regime where the magnetization is stable over a long period of observation. The height and temperature position of this peak result from the distribution of energy barriers in the system, which is mainly controlled by particle size and the intra-particle interactions. Essentially, the peak in the derivative of ΔM signifies the transition from superparamagnetic to blocked state, which is the critical point where the thermal energy is just balanced by the anisotropy energy. At temperatures higher than this peak, particles receive thermal energy sufficient to overcome the anisotropy barrier, causing their magnetic moments to fluctuate and align with the external field randomly (superparamagnetic state). On the other hand, below this peak temperature, thermal agitation is not enough to overcome this anisotropic barrier. Hence, there is a blocking of the magnetic moments, and they are locked in a certain direction (blocked state). The magnetization cannot follow the external magnetic field change and exhibits a hysteresis behavior. In the blocked state, the relaxation time of magnetic moments is longer than the experimental time, and these moments are effectively fixed in a specific orientation. This transition reflects in the peak of the $-\mathrm{d}(\Delta M)/\mathrm{d}T$–$T$ curve, where blocking temperatures are represented. The temperature at which this peak arises provides information about the average particle size in a collection of magnetic nanostructures. Johnston-Peck *et al.* synthesized Ni/NiO core–shell nanoparticles with diameters ranging from 8 nm to 24 nm using a solution-chemistry method.[68] They found that after liquid-phase oxidation, the superparamagnetic T_B of these particles decreased; however, no significant exchange bias was observed. Despite this, the coercivity of the samples increased, indicating a weak exchange bias effect. This was primarily attributed to the amorphous structure of the NiO shell and its thin shell layer, which prevented the spins in NiO from effectively pinning the magnetic moment of the Ni core. This phenomenon is consistent with our study, where the magnetic interactions at the Ni/NiO interface, influenced by particle size, lead to a weak exchange bias effect.

Under low-temperature conditions, the exchange bias effect becomes more pronounced, primarily due to the enhanced thermal stability of the AFM phase in FM/AFM structures. This leads to more stable interfacial spins and, consequently, stronger exchange anisotropy. The Ni/NiO system has a complex atomic interface where local structural irregularities such as interfacial roughness, oxygen vacancy, and strain-induced defect can significantly affect the arrangement of interfacial spins.

The roughness of the Ni/NiO interface is an important factor influencing the strength of interfacial spin coupling. Both theoretical and experimental studies have shown that an increase in interface roughness leads to irregular atomic arrangement at the interface, which in turn induces uneven exchange coupling. Specifically, a rougher interface results in a more complex spin structure, which may cause the spin alignment in the antiferromagnetic NiO layer to deviate from the perfect antiferromagnetic symmetry and form local spin asymmetry. This spin asymmetry leads to a diversity of exchange coupling paths and generates asymmetric exchange effects, thereby enhancing the exchange bias effect.

Oxygen vacancy is a common type of defect in NiO, particularly in Ni/NiO structures, and play a crucial role in enhancing the low-temperature EB effect. The presence of oxygen vacancies disrupts the long-range antiferromagnetic spin order in NiO, creating local spin mismatch regions that form asymmetric exchange coupling paths at the interface. Namely, the introduction of oxygen vacancies alters the local electronic structure of NiO, causing the accumulation or depletion of electrons in certain regions, which results in the distortion of local magnetic moments in the antiferromagnetic NiO layer. Oxygen vacancies make the spins at the interface more stable and promote their freezing at low temperatures, thus strengthening the exchange coupling between FM and AFM layers and enhancing the exchange bias effect.

Strain-induced defect is also significant factor affecting the magnetism of the Ni/NiO interface. In Ni/NiO structures, the lattice constants of the Ni and NiO layers are typically different, creating a strain field at the interface. Strain not only alters the atomic arrangement at the interface but may also affect the stability of interfacial spins through local electronic rearrangements. The local lattice distortions caused by strain can modify the strength and angle of the Ni–O bonds, thereby changing the exchange coupling strength between Ni and NiO. These changes are typically more pronounced at low temperatures, as low temperatures help freeze the spins and reduce thermal fluctuations. So the strain-induced defects can sometimes enhance the asymmetry in the spin alignment at the interface, further boosting the exchange bias effect.

Therefore, the future studies could focus on interfacial regulation strategies, such as elemental doping or interface engineering, combined with microstructural characterization techniques, to further clarify the microscopic mechanisms behind magnetic modulation and improve our understanding of low-temperature EB behavior.

4 Conclusions

C@Ni–NiO nanoparticles were synthesized *via* a homogeneous precipitation method. A comprehensive investigation of their microstructure and magnetic properties was conducted using techniques such as XRD, XPS, SEM, TEM, and SQUID. The magnetic performance of C@Ni–NiO nanoparticles, including the blocking temperature, saturation magnetization, coercivity, coercivity enhancement (ΔH_C), and exchange bias, is influenced by the combined effects of phase proportion and interface phenomena. For the most ideal Ni–NiO composite nanoparticles, weak coupling interactions between the ferromagnetic phase Ni and the antiferromagnetic phase NiO resulted in an exchange bias of 30 Oe at 5 K, accompanied by a coercivity enhancement of 9 Oe. Most of the magnetic behavior can be accounted for by the exchange coupling between ferromagnetic Ni and antiferromagnetic NiO. The *M*–*H* loops and *M*–*T* curves both reveal the presence of a significant degree of spin disorder in the structures, which is far beyond that of simple surfaces in nanoparticles. This spin disorder can reasonably account for the shift in FC loops, indicating the presence of FM–AFM coupling, which can also be corroborated in the $-d(\Delta M)/dT$–T curves, where the sharp steepness at T_B can signify the characteristics of spin freezing.

Data availability

The data that support the findings of this study are available from the corresponding authors (W. Zhong or X. M. He) upon reasonable request.

Author contributions

Zhen-Fei Yu: data curation, formal analysis, investigation, writing – original draft. Kun-Yu Su: investigation, validation. Duan-Qing Chen: formal analysis, visualization. Yu-Ru Ding: methodology, visualization. Yi Zhang: investigation, resources. Wei Zhong: project administration, resources, supervision. Xue-Min He: conceptualization, funding acquisition, investigation, project administration, resources, supervision, writing – review & editing.

Conflicts of interest

There are no conflicts to declare.

Acknowledgements

We would like to thank Engineer Liya Lü of Nanomagnetism Research Group, Nanjing University for SQUID measurement. This work was financially supported by the Scientific Research Foundation of Nanjing University of Posts and Telecommunications (NUPTSF, Grant No. NY220205), the Open Project for National Laboratory of Solid State Microstructures, Nanjing University (Grant No. M30007), and the National Natural Science Foundation (Grant No. 11604160), P. R. China.

References

1 Z. X. Li, Y. F. Guo, H. J. Wang, C. Y. Deng, J. H. Dong, Z. R. Song and Z. K. Li, *Magnetochemistry*, 2023, **9**, 143.
2 H. Tokoro, A. Namai and S. I. Ohkoshi, *Dalton Trans.*, 2021, **50**, 452–459.
3 H. Du, C. Y. Yao, H. Peng, B. Jiang, S. X. Li, J. L. Yao, F. Zheng, F. Yang and A. G. Wu, *Chin. J. Appl. Chem.*, 2022, **39**, 391–406.
4 D. F. Chen and L. Z. Gong, *J. Am. Chem. Soc.*, 2022, **144**, 2415–2437.
5 V. Skumryev, S. Stoyanov, Y. Zhang, G. Hadjipanayis, D. Givord and J. Nogués, *Nature*, 2003, **423**, 850–853.
6 M. Feygenson, Y. Yiu, A. Kou, K. S. Kim and M. C. Aronson, *Phys. Rev. B: Condens. Matter Mater. Phys.*, 2010, **81**, 195445.
7 T. Blachowicz, A. Ehrmann and M. Wortmann, *Nanomaterials*, 2023, **13**, 2418.
8 V. L. Kurichenko, D. Y. Karpenkov and A. Y. Degtyarenko, *J. Magn. Magn. Mater.*, 2023, **565**, 170232.
9 S. Peng, C. Wang, J. Xie and S. H. Sun, *J. Am. Chem. Soc.*, 2006, **128**, 10676–10677.
10 J. B. Tracy, D. N. Weiss, D. P. Dinega and M. G. Bawendi, *Phys. Rev. B: Condens. Matter Mater. Phys.*, 2005, **72**, 064404.
11 B. S. Shivangi and T. Sarkar, *J. Taiwan Inst. Chem. Eng.*, 2020, **113**, 223–230.
12 L. Lei, Z. J. Yao, J. T. Zhou, W. J. Zheng, B. Wei, J. Q. Zu and K. Y. Yan, *Carbon*, 2021, **173**, 69–79.
13 S. K. Mohamed, A. M. Elhgrasi and O. I. Ali, *Environ. Sci. Pollut. Res.*, 2022, **29**, 64792–64806.
14 A. Abdelwahab, F. Carrasco-Marín and A. F. Pérez-Cadenas, *Materials*, 2020, **13**, 3531.
15 A. D. Khalaji, M. Jarosova, P. Machek, K. F. Chen and D. F. Xue, *Scr. Mater.*, 2020, **181**, 53–57.
16 X. J. Xu, X. B. Hou, P. Y. Du, C. H. Zhang, S. C. Zhang, H. L. Wang, A. Toghan and M. H. Huang, *Nano Res.*, 2022, **15**, 7124–7133.
17 H. T. Bai, P. F. Yin, L. M. Zhang, X. Y. Sun and J. W. Dai, *Appl. Phys. A: Mater. Sci. Process.*, 2021, **127**, 1–14.
18 Q. J. Le, T. Wang, S. J. Zhu, J. M. Zhang and Y. X. Zhang, *Funct. Mater. Lett.*, 2016, **9**, 1642002.
19 C. S. Park, K. S. Kim and Y. J. Park, *J. Power Sources*, 2013, **244**, 72–79.
20 C. S. Park, J. H. Kim and Y. J. Park, *J. Electroceram.*, 2013, **31**, 224–230.
21 H. J. Wu, G. L. Wu, Q. F. Wu and L. D. Wang, *Mater. Charact.*, 2014, **97**, 18–26.
22 C. C. Hu, Z. Zhang, T. N. Yang, Y. G. Shi, X. X. Cheng, J. J. Ni, J. G. Hao, W. F. Rao and L. Q. Chen, *Appl. Phys. Lett.*, 2019, **115**, 162402.
23 P. M. Diehm, P. Ágoston and K. Albe, Size-Dependent Lattice Expansion in Nanoparticles: Reality or Anomaly?, *ChemPhysChem*, 2012, **13**, 2443–2454.
24 Z. Q. Wei, T. D. Xia, J. Ma, W. J. Feng, J. F. Dai, Q. Wang and P. X. Yan, *Mater. Charact.*, 2007, **58**, 1019–1024.
25 J. Sheng, C. Rane, U. Welzel and E. J. Mittemeijer, *Phys. E*, 2011, **43**, 1155–1161.
26 B. M. Abu-Zied and A. M. Asiri, *Thermochim. Acta*, 2017, **649**, 54–62.
27 K. Sakamoto, F. Hayashi, K. Sato, M. Hirano and N. Ohtsu, *Appl. Surf. Sci.*, 2020, **526**, 146729.
28 V. G. Prabhu, A. R. Paloly, N. G. Divya and M. J. Bushiri, *Mater. Sci. Eng., B*, 2018, **228**, 132–141.
29 M. R. Salvadori, R. A. Ando, D. Muraca, M. Knobel, C. A. O. Nascimento and B. Corrêa, *RSC Adv.*, 2016, **6**, 60683–60692.
30 O. Kuschel, R. Buss, W. Spiess, T. Schemme, J. Wöllermann, K. Balinski, A. T. N'Diaye, T. Kuschel, J. Wollschläger and K. Kuepper, *Phys. Rev. B*, 2016, **94**, 094423.
31 C. Sun, H. Z. Sun, Z. G. Guo and F. Y. Ge, *J. Mater. Sci.: Mater. Electron.*, 2020, **31**, 20641–20653.
32 M. Patange, S. Biswas, A. K. Yadav, S. N. Jha and D. Bhattacharyya, *Phys. Chem. Chem. Phys.*, 2015, **17**, 32398–32412.
33 N. M. Deraz, *Curr. Appl Phys.*, 2012, **12**, 928–934.
34 K. Sumiyama, A. Monden, R. Katoh, N. Tanaka, D. L. Peng and T. Hihara, *Mater. Trans.*, 2009, **50**, 516–522.

35 X. M. He, Y. R. Xu, X. J. Yao, C. W. Zhang, Y. Pu, X. F. Wang, W. W. Mao, Y. W. Du and W. Zhong, *RSC Adv.*, 2019, **9**, 30195–30206.

36 L. Del Bianco, F. Boscherini, A. L. Fiorini, M. Tamisari, F. Spizzo, M. V. Antisari and E. Piscopiello, *Phys. Rev. B: Condens. Matter Mater. Phys.*, 2008, **77**, 094408.

37 J. Berezovsky, M. H. Mikkelsen, N. G. Stoltz, L. A. Coldren and D. D. Awschalom, *Science*, 2008, **320**, 349–352.

38 M. Kovylina, M. G. del Muro, Z. Konstantinovic, M. Varela, O. Iglesias, A. Labarta and X. Batlle, *Nanotechnology*, 2009, **20**, 175702.

39 S. Chandra, H. Khurshid, W. F. Li, G. C. Hadjipanayis, M. H. Phan and H. Srikanth, *Phys. Rev. B: Condens. Matter Mater. Phys.*, 2012, **86**, 014426.

40 X. L. Sun, N. F. Huls, A. Sigdel and S. H. Sun, *Nano Lett.*, 2012, **12**, 246–251.

41 D. W. Kavich, J. H. Dickerson, S. V. Mahajan, S. A. Hasan and J. H. Park, *Phys. Rev. B: Condens. Matter Mater. Phys.*, 2008, **78**, 174414.

42 S. A. Makhlouf, H. Al-Attar and R. H. Kodama, *Solid State Commun.*, 2008, **145**, 1–4.

43 G. H. Jaffari, M. Bah and S. I. Shah, *J. Alloys Compd.*, 2021, **857**, 157607.

44 B. Kocaman, K. Y. Aktaş and A. C. Basaran, *J. Magn. Magn. Mater.*, 2021, **530**, 167926.

45 M. Ghoshani, M. Mozaffari and A. Al-Nabhani, *Ceram. Int.*, 2021, **47**, 5133–5144.

46 M. Xing, J. Mohapatra, J. Elkins, D. Guragain, S. R. Mishra and J. P. Liu, *Nanoscale*, 2021, **13**, 15837–15843.

47 K. Javed, X. M. Zhang, S. Parajuli, S. S. Ali, N. Ahmad, M. Irfan, J. F. Feng and X. F. Han, *J. Magn. Magn. Mater.*, 2020, **493**, 165738.

48 M. Ghoshani, M. Mozaffari, M. Acet, M. Hosseini and D. Vashaee, *Nanomaterials*, 2023, **13**, 880.

49 M. Ghoshani, M. Mozaafari, P. S. Normile, J. A. De Toro and A. Al-Nabhani, *Magnetochemistry*, 2021, **7**, 40.

50 M. Kowacz, B. Anastaziak, M. Schmidt, F. Stobiecki and P. Kuswik, *Materials*, 2021, **14**, 1237.

51 A. Sharma, J. Tripathi, S. Tripathi, Y. Kumar, K. C. Ugochukwu, D. Kumar, M. Gupta and R. J. Chaudhary, *J. Magn. Magn. Mater.*, 2020, **510**, 166599.

52 A. Kremenovic, B. Jancar, M. Ristic, M. Vucinic-Vasic, J. Rogan, A. Pacevski and B. Antic, *J. Phys. Chem. C*, 2012, **116**, 4356–4364.

53 S. Bhanuchandar, G. Vinothkumar, P. Arunkumar, M. Sribalaji, A. K. Keshri and K. S. Babu, *J. Alloys Compd.*, 2019, **780**, 256–265.

54 M. Patange and S. Biswas, *J. Alloys Compd.*, 2017, **724**, 799–812.

55 A. J. F. Cabral, L. Nascimento, X. Gratens, V. A. Chitta, W. Paschoal and C. M. R. Remédios, *J. Phys. Chem. Solids*, 2021, **159**, 110278.

56 G. M. Al-Senani, F. F. Al-Fawzan, M. Alshabanat, O. H. Abd-Elkader, M. Nasrallah and M. Nasrallah, *Crystals*, 2023, **13**, 1497.

57 N. M. Deraz, *Sci. Sintering*, 2020, **52**, 53–65.

58 V. G. Prabhu, P. S. Shajira, N. Lakshmi and M. J. Bushiri, *J. Phys. Chem. Solids*, 2015, **87**, 238–243.

59 D. R. Cao, L. N. Pan, J. A. Li, X. H. Cheng, Z. Zhao, J. Xu, Q. Li, X. Wang, S. D. Li, J. B. Wang and Q. F. Liu, *Sci. Rep.*, 2018, **8**, 7916.

60 M. Thakur, M. Patra, S. Majumdar and S. Giri, *J. Alloys Compd.*, 2009, **480**, 193–197.

61 H. Ahmadvand, H. Salamati, P. Kameli and F. S. Razavi, *J. Supercond. Novel Magn.*, 2010, **23**, 1467–1471.

62 Z. M. Tian, S. Huang, Y. Qiu, S. L. Yuan, Y. Y. Wu and L. Li, *J. Appl. Phys.*, 2013, **113**, 143906.

63 Q. K. Ong, A. Wei and X. M. Lin, *Phys. Rev. B: Condens. Matter Mater. Phys.*, 2009, **80**, 134418.

64 N. Rinaldi-Montes, P. Gorria, D. Martínez-Blanco, Z. Amghouz, A. B. Fuertes, L. F. Barquín, I. de Pedro, L. Olivif and J. A. Blancoa, *J. Mater. Chem. C*, 2015, **3**, 5674–5682.

65 E. P. Wohlfarth, *Phys. Lett. A*, 1979, **75**, 141–143.

66 C. Binns, M. J. Maher, Q. A. Pankhurst, D. Kechrakos and K. N. Trohidou, *Phys. Rev. B: Condens. Matter Mater. Phys.*, 2002, **66**, 84413.

67 M. D. Mukadam, S. M. Yusuf, P. Sharma, S. K. Kulshreshtha and G. K. Dey, *Phys. Rev. B: Condens. Matter Mater. Phys.*, 2005, **72**, 174408.

68 A. C. Johnston-Peck, J. Wang and J. B. Tracy, *ACS Nano*, 2009, **3**, 1077–1084.